I&EC research
Industrial & Engineering Chemistry Research

Article

pubs.acs.org/IECR

Insight into the Photocatalytic Removal of NO in Air over Nanocrystalline $Bi_2Sn_2O_7$ under Simulated Solar Light

Yanfeng Lu,[†,§] Yu Huang,[*,†,‡] Jun-ji Cao,[*,†,‡] Wingkei Ho,[†,∥] Qian Zhang,[†] Dandan Zhu,[†] and Shun Cheng Lee[⊥]

[†]Key Lab of Aerosol Chemistry and Physics, Institute of Earth Environment, Chinese Academy of Sciences, Xi'an 710061, China

[‡]State Key Lab of Loess and Quaternary Geology (SKLLQG), Institute of Earth Environment, Chinese Academy of Sciences, Xi'an 710061, China

[§]University of Chinese Academy of Sciences, Beijing 100049, China

[∥]Department of Science and Environmental Studies, The Hong Kong Institute of Education, Hong Kong, China

[⊥]Department of Civil and Environmental Engineering, The Hong Kong Polytechnic University, Hung Hom, Kowloon, Hong Kong, China

Supporting Information

ABSTRACT: Understanding the photocatalytic conversion mechanism of NO is crucial to develop an effective and practical strategy for indoor air pollution control. In this study, we systematically investigated the photocatalytic removal mechanism of NO over nanocrystalline $Bi_2Sn_2O_7$, which was successfully synthesized via hydrothermal method using bismuth citrate and stannic chloride pentahydrate as precursors for the first time. Various characterizations were carried out to study the physicochemical properties of the as-prepared samples. The performance of the as-prepared $Bi_2Sn_2O_7$ samples was evaluated by the photocatalytic degradation of NO in a continuous reactor under simulated solar light irradiation. The NO removal rate over the $Bi_2Sn_2O_7$ sample synthesized for 12 h (BSO-12) was 37%, which was much higher than those of $Bi_2Sn_2O_7$ samples synthesized for 24 h (BSO-24) and 36 h (BSO-36). Results from photocurrent tests and electrochemical impedance spectroscopy (EIS) demonstrated that the BSO-12 sample presents much more effective interface charge separation efficiency, which can contribute to its improved photocatalytic performance. Reactive radicals during the photocatalysis processes were identified via trapping experiments, which were also confirmed by electron spin resonance (ESR) study. Combined with the quantification of reaction intermediates, the photocatalytic removal mechanism of NO over nanocrystalline $Bi_2Sn_2O_7$ was proposed for the first time.

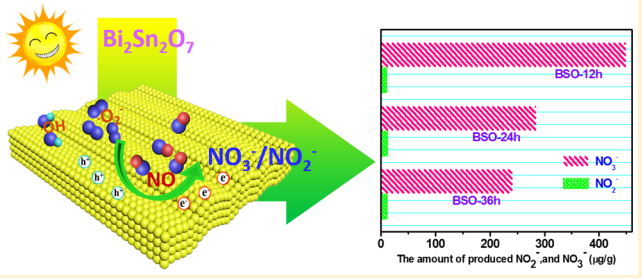

1. INTRODUCTION

Indoor air quality (IAQ) has received increasing attention in recent years because of its potential effect on human health.[1] Gaseous pollutants such as nitrogen oxides (NO_x), sulfur dioxide (SO_2), and volatile organic compounds (VOCs) are common indoor air pollutants.[2] Studies showed that the concentrations of many indoor air pollutants are even higher than those outdoors, which can be attributed to the presence of emission sources in indoor environment.[3−5] Among these pollutants, NO_x is one of the most common gaseous pollutants found in indoor environment.[6] Long-term exposure to NO_x may cause sick building syndrome, which refers to the symptoms including eyes and throat stimulus, stuffy nose, and headache.[7] Traditional methods such as physical adsorption and biofiltration are not economically feasible at low pollutant concentrations of part-per-billion (ppb) levels, which are typical concentrations for indoor air pollutants.[8] Therefore, highly efficient technologies that can be operated at room temperature with low cost for eliminating NO_x are urgently needed.

Semiconductor photocatalysis is an innovative and promising technique for NO_x removal because it can use inexhaustible solar light energy to mitigate air pollution problems. A number of studies have reported the degradation of NO_x using the photocatalytic technique.[9−12] Among various oxide semiconductor photocatalysts, TiO_2-based nanomaterials have been studied intensively for their intrinsic redox properties.[13−15] However, TiO_2 can only absorb UV light, which accounts for less than 5% of solar light energy due to its large band gap energy (3.2 eV for anatase).[16] Therefore, much effort has been focused on designing visible-light-driven photocatalysts to enhance the efficiency of utilizing solar energy.

Received: July 1, 2016
Revised: September 13, 2016
Accepted: September 19, 2016
Published: September 19, 2016

DOI: 10.1021/acs.iecr.6b02514
Ind. Eng. Chem. Res. 2016, 55, 10609−10617

Bismuth-containing photocatalysts, such as Bi_2WO_6,[12] Bi_2MoO_6,[17] and $BiVO_4$,[18] have been studied extensively because of their high activities and nontoxicity for environmental applications. Their visible-light-driven activity can be ascribed to the orbital hybridization of O 2p and Bi 6s.[19]

Bismuth stannate ($Bi_2Sn_2O_7$) is a type of Bi-based semiconductor material that has received considerable interest in catalysis, gas sensors, and optoelectronic devices in recent years.[20,21] $Bi_2Sn_2O_7$, which has a typical pyrochlore structure and dispersed valence band, can facilitate the mobility of charged carriers and narrow the band gap.[20] In addition, the hybridization states Bi $6s^26p^0$, Sn $5s^05p^0$, and a small amount of O 2p comprise the valence band maximum (VBM) and conduction band minimum (CBM) of $Bi_2Sn_2O_7$. On the one hand, the dispersed s and p orbitals guarantee small effective masses for electrons and holes, which make them easily transferred to the surface of the photocatalyst. On the other hand, the hybridized interactions between Bi and Sn lead to highly dispersed VBM and CBM electronic configurations to enhance the mobility of photogenerated holes and electrons.[20] $Bi_2Sn_2O_7$ has been synthesized via different methods as reported in previous studies. For example, Walsh et al.[19] synthesized polycrystalline $Bi_2Sn_2O_7$ using solid-state reaction methods at 1100 °C and performed an electronic structure study by gradient corrected density functional theory and an experimental approach. Tian et al.[21] prepared polycrystalline $Bi_2Sn_2O_7$ using bismuth nitrate and potassium stannate as precursors using a hydrothermal route and $Bi_2Sn_2O_7$ for photocatalytic removal of As(III). $Bi_2Sn_2O_7$ has been applied as a potential catalyst for the removal of organic compounds, different types of dyes, and water splitting.[22] However, $Bi_2Sn_2O_7$ has scarcely been studied for indoor air pollution control, especially for the abatement of gaseous NO_x.

In this work, nanocrystalline $Bi_2Sn_2O_7$ samples were synthesized by a facile hydrothermal route under different reaction times using bismuth citrate and stannic chloride pentahydrate as precursors for the first time. The involvement of citrate ions during the synthesis processes can facilitate the formation of nanoparticles in view of complexation. Under simulated solar light irradiation, the nanocrystalline $Bi_2Sn_2O_7$ exhibited high photocatalytic activity on the removal of NO. The characterization results showed that bismuth citrate as a source of Bi^{3+} greatly influenced the chemical and physical properties of $Bi_2Sn_2O_7$. The role of active species during the photocatalytic processes was also investigated in detail. Moreover, a reasonable mechanism for the photooxidation of NO over $Bi_2Sn_2O_7$ has been proposed.

2. EXPERIMENTAL SECTION

2.1. Synthesis of Nanocrystalline $Bi_2Sn_2O_7$. Nanocrystalline $Bi_2Sn_2O_7$ samples were prepared by a facile one-pot hydrothermal process using bismuth citrate ($C_6H_5BiO_7$) and stannic chloride ($SnCl_4{\cdot}5H_2O$) as precursors. All the chemicals employed in this study were of analytical grade and used without further purification. Bismuth citrate was obtained from Sigma-Aldrich, and other chemicals used in the experiment were purchased from Sinopharm Chemical Reagent Co., Ltd. (Shanghai, China). Deionized water was provided by Millipore Milli-Q water purification system. (Shanghai, China).

For the synthesis of $Bi_2Sn_2O_7$, $SnCl_4{\cdot}5H_2O$ (1 mmol) was first dissolved in 35 mL of NaOH solution (1.0 mol L^{-1}) and stirred for a short time. Bismuth citrate (1 mmol) was added to the above solution under vigorous stirring for 30 min. The forming white suspension was transferred into a 50 mL Teflon-lined stainless steel autoclave maintained at 180 °C for 12 h and cooled down to room temperature naturally. The products were collected by centrifugation, rinsed several times with deionized water and absolute ethanol, and dried at 80 °C. To investigate the effect of reaction time on the properties of $Bi_2Sn_2O_7$, hydrothermal synthesizes at 24 and 36 h under other identical conditions with those of the sample synthesized at 12 h were also conducted. The resulting samples synthesized at 12 h, 24 h, and 36 h were denoted as BSO-12, BSO-24, and BSO-36, respectively.

2.2. Characterization. Powder X-ray diffraction (XRD) was performed with a Philips X'pert PRO SUPER diffractometer using Cu Kα (λ = 0.154 06 nm) radiation at 40 kV and 40 mA with a scanning rate of 0.04° 2θ/s in the 2θ range of 10°−80°. The morphology of the samples was characterized by field emission scanning electron microscopy (SUPRA 55, Japan) and transmission electron microscopy (TEM, JEM-2010, Japan). The Fourier transform infrared spectroscopy (FTIR) spectra were recorded on an FTIR absorption spectrometer (Magna-IR 750, Nicolet, USA), with KBr as the diluent. The Brunauer−Emmett−Teller (BET) surface area and pore structure of the $Bi_2Sn_2O_7$ samples were obtained from N_2 adsorption/desorption isotherms at 77 K using an ASAP 2020 automatic analyzer (Micromeritics Instrument Corp., Norcross, GA, USA). A Varian Cary 100 Scan UV−visible system equipped with a Labsphere diffuse reflectance accessory was used to obtain the reflectance spectra of the catalysts over a range of 200−800 nm. Labsphere USRS-99-010 was employed as a reflectance standard. The spectra were converted from reflection to Kubelka−Munk spectral function by the Kubelka−Munk method. The samples for electron spin resonance (ESR) spectroscopy (ER200-SRC, Bruker, Germany) were prepared by mixing 0.05 g of the as-prepared photocatalyst in a 25 mM 5,5′-dimethyl-1-pirroline *N*-oxide (DMPO) solution with a 50 mL aqueous dispersion for DMPO-·OH or a 50 mL methanol dispersion for DMPO-·O_2^-. The light irradiation source was a 300 W Xe arc lamp (PLS-SXE 300, Beijing, China).

After the photocatalytic activity test was completed, intermediates and final products (nitrate and nitrite ions) remaining on the catalyst powders were extracted by immersing the powders into deionized water (10 mL) and measured with a Dionex-600 ion chromatograph (Dionex Inc., Sunnyvale, CA, USA) equipped with an IonPac AS14A column. The mobile phase was composed of a mixture of 1.8 mM Na_2CO_3 and 1.7 mM $NaHCO_3$ at a flow rate of 1.20 mL min^{-1}, and the injected sample volume was 20 μL. The detection limit for NO_2^- and NO_3^- was 5 μg L^{-1} and 25 μg L^{-1}, respectively.

2.3. Photoelectrochemical Characterization. The photoelectrochemical properties of BSO-12, BSO-24, and BSO-36 were evaluated using a Parstat4000 electrochemical workstation (USA) in a conventional three-electrode cell, in which a platinum plate and an Ag/AgCl electrode were used as counter electrode and reference electrode, respectively. To fabricate the working electrode, 45 mg of $Bi_2Sn_2O_7$ was dispersed into 5 mL of Nafion ethanol solution to obtain a homogeneous suspension through bath sonication. $Bi_2Sn_2O_7$ films were modified on the fluorine-doped tin oxide conductive glass by dip coating and then dried at room temperature. The photocurrent−time curves were measured at 0.2 V versus Ag/AgCl in 0.5 mol L^{-1} Na_2SO_3 at ambient temperature under irradiation with a 300 W Xe arc lamp. Electrochemical impedance spectroscopy (EIS) was conducted at a frequency

DOI: 10.1021/acs.iecr.6b02514
Ind. Eng. Chem. Res. 2016, 55, 10609−10617

range of 0.1 Hz to 100 kHz with a 5 mV voltage amplitude under open-circuit voltage in 1 mmol L^{-1} $K_3Fe(CN)_6$ and $K_4Fe(CN)_6$ solution. The flat band potential was measured through Mott−Schottky plots at a frequency of 1 kHz in 0.1 mol L^{-1} Na_2SO_4.

2.4. Photocatalytic Activity Test. The photocatalytic activity of the as-prepared samples was evaluated for the removal of NO at the ppb level performed at ambient temperature in a continuous flow reactor. The volume of the rectangular reactor with a quartz glass on the surface, which was made of stainless steel composites, was 4.5 L (30 cm × 15 cm × 10 cm). A sample dish containing the photocatalyst powders was placed in the center of the reactor. Each sample (0.20 g) was dispersed in deionized water (15 mL) via ultrasonic processing for 10 min and then poured into glass dishes (R = 9.0 cm). The dishes containing the samples were treated at 70 °C for several hours until complete removal of water in the suspension was achieved. The dishes were then cooled to room temperature before use. A commercial 300 W Xe arc lamp (MICROSOLAR 300 UV, Beijing) for the simulated solar light photocatalytic activity test was vertically placed 20 cm above the reactor. The wavelength of the simulated solar-light ranges from 200 to 1100 nm, and the associated spectra composition of the light source were shown in Figure S1 in Supporting Information. The NO gas was acquired from a compressed gas cylinder at a concentration of 50 ppm of NO (N_2 balance). The initial concentration of NO was diluted to about 400 ppb via air streaming. A gas mixture of 400 ppb NO was fed into the reactor system at 3.0 L min^{-1}. The whole measurement was conducted at ambient conditions and relative humidity of 30 ± 5%. After adsorption−desorption equilibrium among catalysts, gases and water vapor were obtained, and the lamp was turned on. The concentrations of NO, NO_2, and NO_x were continuously measured every 1 min by a NO_x analyzer (Ecotech, 9841), which monitored NO, NO_2, and NO_x (NO_x = NO + NO_2) with a sampling rate of 0.6 L min^{-1}.

In the data analysis, the removal ratio (η) of NO and the yield of NO_2 were calculated according to the following equation:

$$\eta\ (\%) = \frac{C_o - C}{C_o} \times 100$$

$$NO_2\ \text{yield}\ (\%) = \frac{C_{NO_2}}{C_o - C} \times 100$$

where η is the NO removal rate, C is the outlet concentration of NO of each access gas for 1 min, C_{NO_2} represents the production of NO_2, and C_o represents the inlet concentration after achieving adsorption−desorption equilibrium.

2.5. Trapping Experiments of Active Species. We used potassium iodide (KI) and *tert*-butyl alcohol (TBA) as effective scavengers of h^+ and ·OH, respectively. Potassium dichromate ($K_2Cr_2O_7$) was utilized as a photogenerated electron scavenger. Each sample (0.20 g) with different trapping agents was dispersed in deionized water (15 mL), ultrasonically dispersed for 20 min, and poured into glass dishes (R = 9.0 cm). The dishes that coated the samples were treated at 70 °C for several hours in an oven. Finally, the dried dishes were utilized for further photocatalytic NO removal tests.

3. RESULTS AND DISCUSSION

3.1. Phase Structure and Morphology. The XRD patterns of $Bi_2Sn_2O_7$ synthesized at different reaction times are shown in Figure 1. All the strong diffraction peaks could be

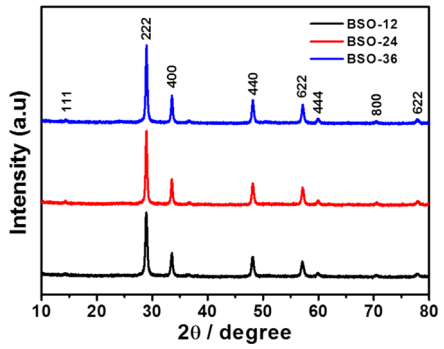

Figure 1. XRD patterns of the $Bi_2Sn_2O_7$ samples synthesized at different reaction times.

readily indexed to a pure cubic phase of $Bi_2Sn_2O_7$ (JCPDS No. 87-0284) with a space group of $Fd\bar{3}m$ (No. 227).[21] No impurity peaks were observed in these patterns, indicating the high purity of the $Bi_2Sn_2O_7$ products. The intense and sharp diffraction peaks suggested that the as-synthesized products were well crystallized. Moreover, the intensity of the diffraction peaks strengthened with the increase of synthesis time, thereby illustrating that the prolonged synthesis time could promote $Bi_2Sn_2O_7$ growth.[23] In order to compare the material differences of performance obtained from shorter time, the BSO-8 was synthesized at 180 °C for 8 h. However, the shorter time cannot obtain pure $Bi_2Sn_2O_7$ while the $SnCl_4{\cdot}5H_2O$ completely fail to react (as shown in Figure S2). The average size of $Bi_2Sn_2O_7$ crystallite was also calculated from the (222) peak by the Scherrer equation.[24] As shown in Table S1, the estimated particle sizes of BSO-12, BSO-24, and BSO-36 were 18, 25, and 30 nm, respectively, suggesting that the crystallite size increased accordingly with the increase in reaction time. Moreover, the IR spectra of the BSO-12, BSO-24, and BSO-36 samples recorded in the range of 400−4000 cm^{-1} are shown in Figure S3. The experimental results revealed that the band at about 625 cm^{-1} was ascribed to the Sn−O stretching vibration in the BO_6 octahedron, and the weak band of 513 cm^{-1} was assigned to the stretching vibration of Bi−O−Bi bonds.[25] The IR-active optic modes from the vibration and bending of metal−oxygen bonds in the IR spectra of BSO-12, BSO-24, and BSO-36 indicated that all the samples were high purity products.

Scanning electron microscopy (SEM) and transmission electron microscopy (TEM) characterizations were performed to understand the morphological and structural characteristics of the as-prepared $Bi_2Sn_2O_7$ samples. As shown in Figure 2a, the BSO-12 sample was composed of irregular spheres with diameter less than 500 nm, which formed via the combination of nanocrystalline $Bi_2Sn_2O_7$ (shown in the inset magnified SEM image). As the hydrothermal synthesis time increased from 12 to 36 h, the morphological structures of the $Bi_2Sn_2O_7$ samples varied significantly (Figure 2a and Figure S4a,b), but all of them formed via the aggregation of nanocrystalline $Bi_2Sn_2O_7$ (inset magnified images). The results demonstrated that the final $Bi_2Sn_2O_7$ samples consisted of nanocrystallines, which eventually assembled to different morphologies under different

DOI: 10.1021/acs.iecr.6b02514
Ind. Eng. Chem. Res. 2016, 55, 10609−10617

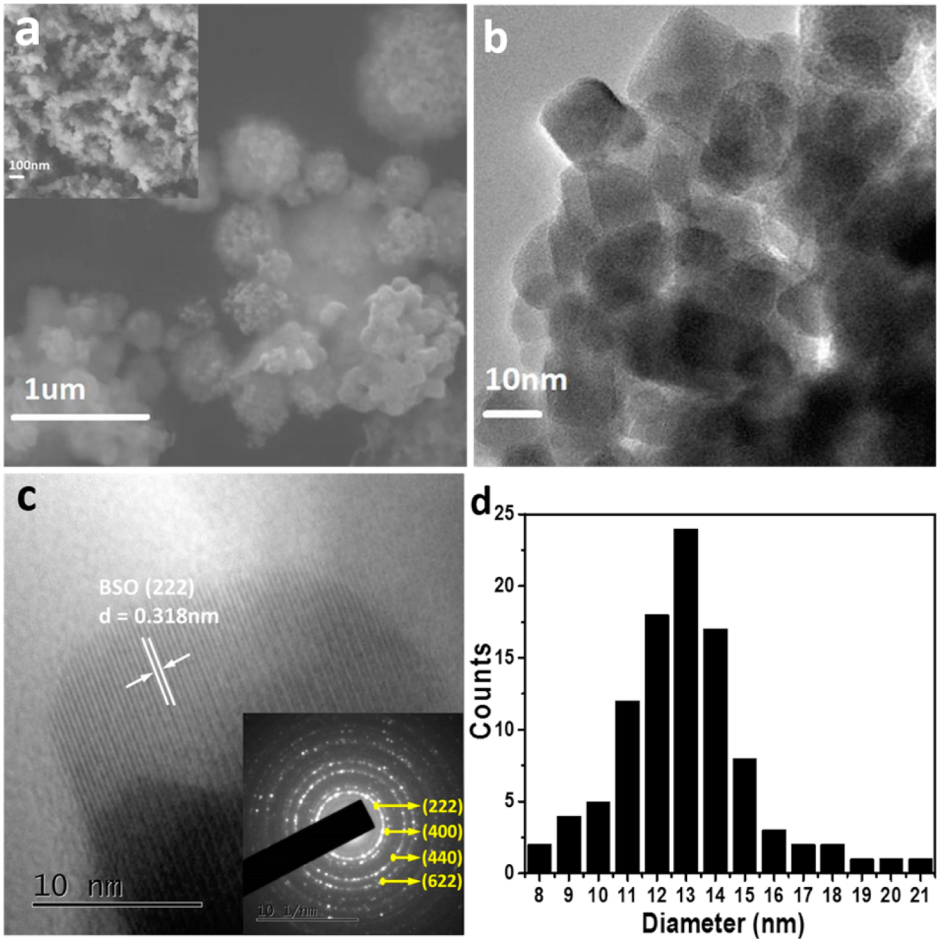

Figure 2. (a) SEM images, (b) low-magnification TEM image, (c) high-resolution TEM images of BSO-12 (inset is SAED image of BSO-12), and (d) particle size distributions of the BSO-12 sample obtained by measuring the length of the side of 100 particles.

reaction times. The inset magnified images suggested that the particle size of the $Bi_2Sn_2O_7$ samples increased with the increase in reaction time, which was consistent with the XRD results.

The morphological structure of the BSO-12 sample was further characterized by TEM. As shown in Figure 2b, the BSO-12 sample consisted of nanoparticles with a size of approximately 10−20 nm, which was consistent with the SEM and XRD calculation results. The high-resolution TEM image in Figure 2c exhibits continuous and well-resolved lattice fringes, with *d*-spacing of ∼0.318 nm corresponding to the (222) plane of $Bi_2Sn_2O_7$.[21] Multidiffraction rings instead of dots were observed in the inset of Figure 2c, suggesting that the hydrothermally synthesized BSO-12 sample possessed a polycrystalline nature. Figure 2d shows the particle size distribution of the BSO-12 sample by measuring the dimensions of 100 particles, and the results demonstrated that the dominant particle size of $Bi_2Sn_2O_7$ was 13 nm.

3.2. Specific Surface Area and Pore Structures. Table S1 shows the specific surface areas and pore sizes of the $Bi_2Sn_2O_7$ samples. The BET surface areas of BSO-12, BSO-24, and BSO-36 were 15, 10, and 9 m^2/g, respectively. The pore sizes of these samples varied with the surface areas. The obvious decreases in the surface area and pore size of BSO-24 and BSO-36 were associated with morphological changes and increased particle sizes. Generally, high surface area could promote the mass transfer of gas pollutants or reaction intermediates during the photocatalytic reaction processes. The high surface area and high mass transfer efficiency of our products were expected to enhance photocatalytic activity.

3.3. Optical Absorption. UV−vis diffuse reflectance spectroscopy (DRS) was performed to characterize the electronic states of the as-prepared samples. Figure 3 shows the UV−vis spectra of the BSO-12, BSO-24, and BSO-36

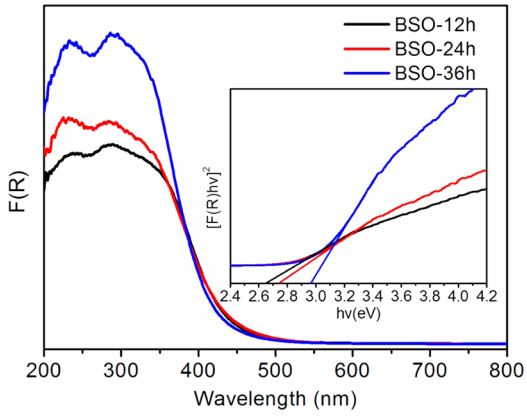

Figure 3. DRS of the as-prepared $Bi_2Sn_2O_7$ samples. Data are plotted as transformed Kubelka−Munk function $F(R)$ versus the wavelength of light. Inset shows the plots of $[F(R)h\nu]^2$ versus photon energy to determine the direct transition energies of the final products.

DOI: 10.1021/acs.iecr.6b02514
Ind. Eng. Chem. Res. 2016, 55, 10609−10617

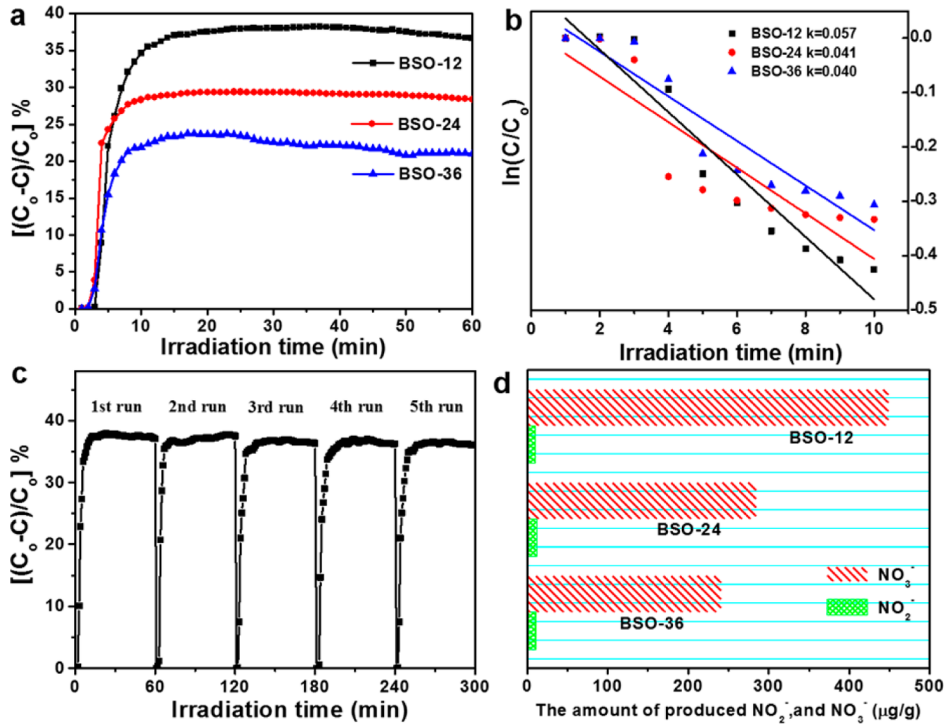

Figure 4. (a) NO photocatalytic degradation under solar light irradiation for different $Bi_2Sn_2O_7$ samples, (b) plots of the dependence of $\ln(C/C_o)$ on irradiation time, (c) photochemical stability of the BSO-12 sample, and (d) amount of produced NO_2^- and NO_3^-.

samples. The inset plots show the optical absorption edges (in eV) of the $Bi_2Sn_2O_7$ samples. As shown in Figure 3, all the samples exhibited absorption bands in the visible light region. The steep shape of the spectrum indicated that visible light absorption was due to the band gap transition.[26] The absorption edge of BSO-36 blue-shifted (shifted to shorter wavelengths) compared with those of BSO-12 and BSO-24, which may be caused by the particle size effect.[27−30] The band gap energies estimated from $[F(R)h\nu]^2$ versus photon energy plots are summarized in Table S1. The optical band gaps were 2.65, 2.75, and 2.96 eV for BSO-12, BSO-24, and BSO-36, respectively. These findings suggested the beneficial optical (light absorption and scattering) and electrical properties of $Bi_2Sn_2O_7$ at effective particle sizes. Therefore, visible light absorption ability makes nanocrystalline $Bi_2Sn_2O_7$ a promising photocatalyst for solar-driven applications.

4. PHOTOCATALYTIC PERFORMANCE ON NO DEGRADATION

The photocatalytic efficiency of the as-prepared $Bi_2Sn_2O_7$ samples was evaluated by the degradation of NO under simulated solar light irradiation in a continuous reactor. Figure 4a shows the variation in NO removal rate ($[(C_o - C)/C_o]$ %) with irradiation time over the obtained $Bi_2Sn_2O_7$ samples. C_o is the initial concentration of NO, and C is the concentration of NO after photocatalytic degradation for time t. As previously reported, NO can barely be photolyzed under light irradiation without photocatalysts.[11] As shown in Figure 4a, the NO concentration drastically decreased after the simulated solar light was turned on, and it reached a steady state after about 10 min. The NO removal rate over the BSO-12 sample reached 37%, which was much higher than those over BSO-24 (28%) and BSO-36 (23%). The NO conversion rate and NO_2 yield over the samples are contrasted in Figure S5. The BSO-12 showed superior performance in NO conversion with lower NO_2 yield. Apparently the production of NO_2 intermediate was efficiently inhibited over the BSO-12 sample, which displayed much higher selectivity than BSO-24 and BSO-36. Here we suppose that the lower yield of NO_2 generated from BSO-12 under irradiation is due to the superior charge separation and rich amount of strong oxidative species. For an obviously quantitative comparison, we used the Langmuir−Hinshelwood model to describe the rates of the photocatalytic removal of NO.[9] Notably, the initial photocatalytic degradation of NO was recognized to follow mass transfer controlled first-order kinetics comparatively as a result of low-concentration target pollutants, as evidenced by the linear plot of $\ln(C/C_o)$ versus photocatalytic reaction time t. Figure 4b shows that the initial rate constant of NO degradation over BSO-12 under simulated solar light irradiation was estimated as 0.057 min^{-1}, which was faster than that over BSO-24 (0.041 min^{-1}) and BSO-36 (0.040 min^{-1}). These observations indicated that the reaction time during synthesis significantly affected the photocatalytic activity of the $Bi_2Sn_2O_7$ samples because of its influence on the photocatalyst microstructure, as evidenced by XRD, SEM, and TEM characterizations.

To further study the stability of the $Bi_2Sn_2O_7$ samples on the photocatalytic oxidation of NO in gas phase, we carried out multiple runs of the photocatalytic experiment with the $Bi_2Sn_2O_7$ samples. Interestingly, the $Bi_2Sn_2O_7$ samples only exhibited slight deactivation after five cycles of repeated experiments. The slight decrease in activity was due to the accumulation of NO_3^- on the catalyst surface, resulting in the deactivation of the photocatalysts.[26,31] The stability of $Bi_2Sn_2O_7$ was further confirmed via XRD. As shown in Figure S6, the crystal structure of the used photocatalyst did not change after the photocatalytic reaction with NO, which suggested its phase stability. The produced amounts of NO_2^- and NO_3^- on the surfaces of the $Bi_2Sn_2O_7$ samples after the photoactivity test

DOI: 10.1021/acs.iecr.6b02514
Ind. Eng. Chem. Res. 2016, 55, 10609−10617

were determined by ion chromatography. Figure 4d shows a plot of the amount of produced NO_2^- and NO_3^- which was estimated by the following equation: the amount of $[NO_3^-(\mu g/g)] = [C_{measured}\ (NO_3^-) \times 10]/0.2$. The amount of NO_3^- on the BSO-12 surfaces was the highest at 449.77 μg/g, followed by those on BSO-24 (284.75 μg/g) and BSO-36 (241.29 μg/g). This trend was consistent with the photocatalytic activity of the three $Bi_2Sn_2O_7$ samples. Moreover, an unstable intermediate NO_2^- which was estimated using the above methods showed only a weak signal in the samples, probably because of the presence of some active species with strong redox potential, which can oxidize the majority of NO into NO_3^-. These results provide an accurate estimation of the final products from NO degradation by the nanocrystalline $Bi_2Sn_2O_7$. These results demonstrated that the $Bi_2Sn_2O_7$ samples are promising for air purification under solar light irradiation.

5. INSIGHTS INTO THE ENHANCED PHOTOCATALYTIC DEGRADATION MECHANISM OF NO

The above experimental results demonstrated that the BSO-12 sample showed superior photocatalytic activities to the BSO-24 and BSO-36 samples under simulated solar light irradiation. In general, the photocatalytic activity is closely related to the generation, separation, migration efficiency, and oxidation−reduction ability of the photogenerated charge carriers.[32]

Photocurrent is effective in characterizing the generation, separation, and migration efficiency of photocarriers.[33] As shown in Figure 5a, steady and prompt photocurrent generation was obtained over all the $Bi_2Sn_2O_7$ samples during the on and off cycles under simulated solar light irradiation. Notably, the intensity of the photocurrent produced over the BSO-12 sample was the highest among the three $Bi_2Sn_2O_7$ samples, which exhibited a positive correlation with the photocatalytic activity. The superior photocurrent production ability of BSO-12 was attributed to the shorter migration distance of carriers because of the largest surface area and smallest particle size of BSO-12, as characterized by XRD and SEM. The interface charge separation efficiency was investigated by the EIS spectra (Nyquist plots). A small arc radius suggests high efficiency of charge transfer.[21] As shown in Figure 5b, the radius of BSO-12 was the smallest among the three samples, indicating that the charge transfer efficiency of BSO-12 was the highest, which was consistent with the photoluminescence characterization results (Figure S7). Obviously, the BSO-12 sample displayed the lowest intensity, which suggested that it possessed the highest separation efficiency of charge carriers. These results implied that the small BSO-12 nanoparticles could effectively improve the separation efficiency of photogenerated electron−hole pairs and charge migration. An increase in the arc radius was observed with the prolonged synthetic time. The superior charge transfer rate of BSO-12 was attributed to its small particle size, high specific surface area, and large dipole moment.

A proper band structure is essential for the photocatalytic oxidation/reduction ability of photocatalysts.[34] Figure 5c shows the typical Mott−Schottky plots ($1/C^2$ versus voltage (V/SCE)) for the BSO-12 sample. The slope of the curve provided the flat band potential (V_{fb}), which plays an important role in deciding photocatalytic performance.[35] The V_{fb} value of BSO-12 was estimated at −0.81 V versus Ag/AgCl at pH 6.8 (equivalent to −0.61 eV vs NHE at pH 6.8). Thus, E_{CB} of BSO-12 was −0.61 eV, and the valence band potential (E_{VB}) of BSO-12 was 2.06 eV based on the measured band gap energy (E_g = 2.67 eV) of BSO-12 from UV−vis DRS measurements (Figure 3). E_{CB} (−0.61 eV) of BSO-12 was more negative than that of the redox potential of $O_2/\cdot O_2^-$ (−0.33 eV vs NHE),[36] suggesting that the photoexcited electrons in the conduction band could reduce O_2 to $\cdot O_2^-$. However, E_{CB} of BSO-12 was 2.65 eV, which was more negative than the redox potential of E^0 ($OH^-/\cdot OH$, +2.38 eV).[21,37] These analyses demonstrated that the production of $\cdot O_2^-$ radicals during the photocatalysis processes over the as-prepared BSO-12 samples was thermodynamically favorable, whereas the formation of ·OH radical was thermodynamically not allowed.

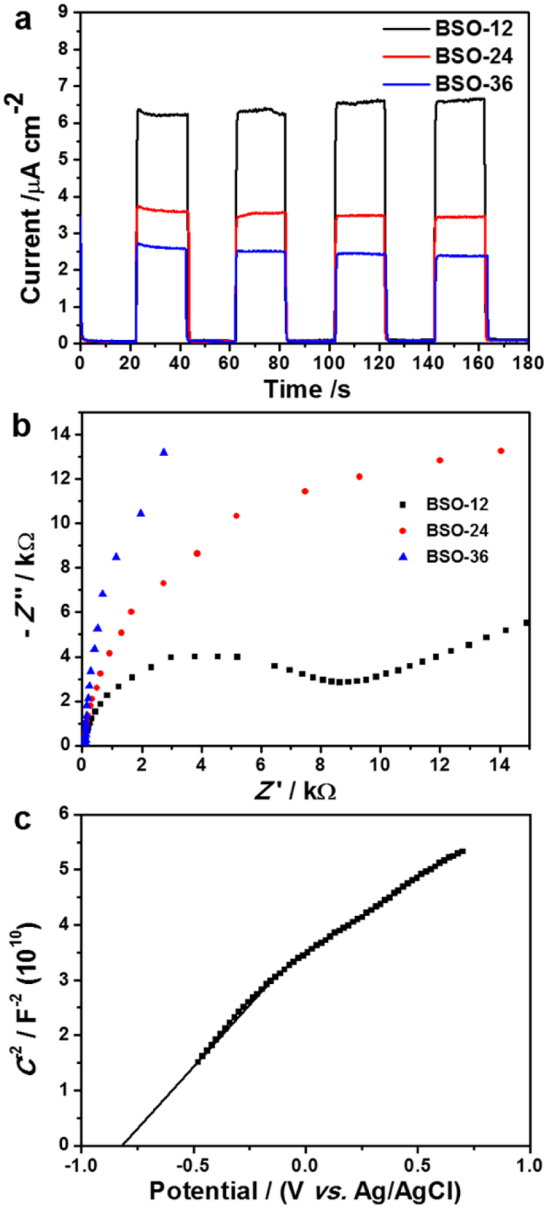

Figure 5. (a) Photocurrent transient responses with a 300 W Xe arc lamp for BSO-12, BSO-24, and BSO-36 in 0.1 M Na_2SO_4 solution at 0.2 V versus Ag/AgCl; (b) EIS Nyquist plots of BSO-12, BSO-24, and BSO-36 in a 5.0 mM $[Fe(CN)_6]^{3-/4-}$ solution under simulated solar light; and (c) Mott−Schottky plots of the BSO-12 sample.

Radical trapping experiments were conducted to identify the active radical species in the photocatalytic NO degradation processes over the $Bi_2Sn_2O_7$ samples. Scavengers, such as KI

DOI: 10.1021/acs.iecr.6b02514
Ind. Eng. Chem. Res. 2016, 55, 10609−10617

(1%), TBA (1%), and potassium dichromate ($K_2Cr_2O_7$, 1%), were used to trap hole (h^+), hydroxyl radical (·OH), and electron (e^-), respectively. As shown in Figure 6a, the

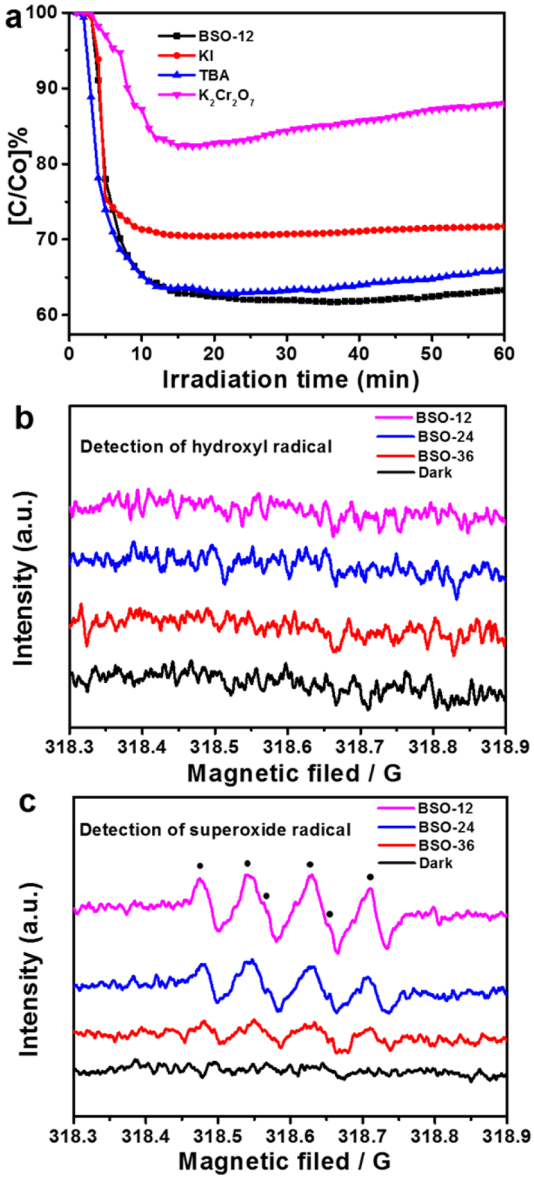

Figure 6. (a) Active species trapping of BSO-12. DMPO-ESR spin trapping spectra for the detection of ·OH (b) and $\cdot O_2^-$ (c) in aqueous solution under simulated solar light irradiation.

photocatalytic activity of NO degradation over the BSO-12 sample showed insignificant variation after the addition of TBA scavenger, which confirmed that ·OH radicals were not involved in the photocatalytic processes. However, with the addition of scavenger $K_2Cr_2O_7$, the NO removal rate over BSO-12 was reduced to 18%, which was reduced by 2 times as compared with the original removal rate (37%). Thus, the photoactivated electrons played an important role in NO removal. Moreover, photocatalytic activity was also inhibited with the introduction of scavenger KI, indicating that h^+ was also involved in the photocatalytic NO degradation processes. These radical trapping results were consistent with the aforementioned band structure analysis.

The DMPO-ESR method was adopted for the direct identification and quantification of short-lived ·OH and $\cdot O_2^-$ radicals during the photodegradation of NO over the as-prepared $Bi_2Sn_2O_7$ samples with DMPO as the spin trapping reagent under simulated solar light irradiation. As shown in Figure 6b and Figure 6c, the characteristic ESR signals of ·OH and $\cdot O_2^-$ radicals were absent under dark conditions. The signals assigned to ·OH radicals were not observed as in Figure 6b, whereas $\cdot O_2^-$ radicals were detected in the as-prepared samples under simulated solar light irradiation (Figure 6c). The signal of $\cdot O_2^-$ radicals for BSO-12 was much stronger than those for BSO-24 and BSO-36. This result also suggested that BSO-12 could produce more radicals, which was responsible for its enhanced photocatalytic activity.

Therefore, based on the above analysis, the $\cdot O_2^-$ radicals and holes were the predominant reactive oxidation species during photocatalytic NO removal over $Bi_2Sn_2O_7$ samples under simulated solar light irradiation. The BSO-12 sample could produce more intensive active species, which resulted in its superior photocatalytic activity compared with BSO-24 and BSO-36. This finding was attributed to the intrinsic properties of BSO-12, such as small particle size, superior light absorption ability, and high surface area. A possible photocatalytic reaction mechanism for NO removal over the $Bi_2Sn_2O_7$ samples under simulated solar light irradiation was proposed, as shown in Figure 7. The photodegradation mechanism of NO involves a

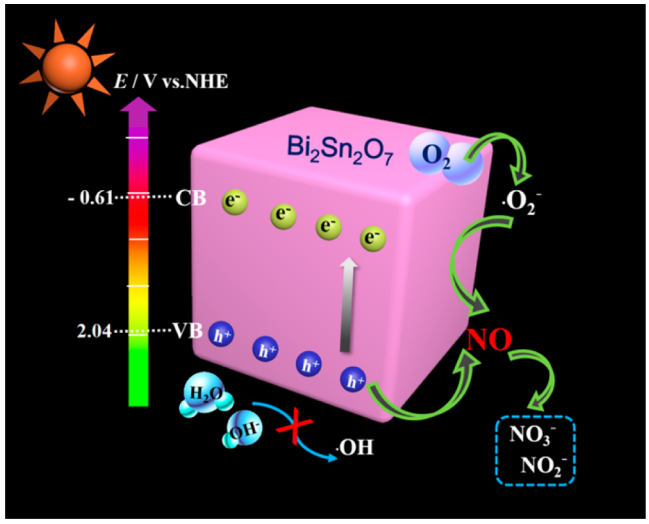

Figure 7. Schematic diagram of the photocatalytic degradation mechanism of NO with the as-prepared $Bi_2Sn_2O_7$ samples under simulated solar light irradiation.

battery of processes.[38,39] First, NO is adsorbed on the surface of the photocatalyst until adsorption−desorption equilibrium achieved. The photocatalytic oxidation of gaseous NO has been proposed to involve the reactions displayed in eqs 1−4, in which nitrogen monoxide reacted with reactive radicals producing NO_2^- and NO_3^-, which can be formed by the following processes:

$$BSO + h\nu \rightarrow e^-(BSO) + h^+(BSO) \quad (1)$$

$$e^-(BSO) + O_2 \rightarrow \cdot O_2^- \quad (2)$$

$$NO_x + \cdot O_2^- \rightarrow NO_3^-/NO_2^- \quad (3)$$

DOI: 10.1021/acs.iecr.6b02514
Ind. Eng. Chem. Res. 2016, 55, 10609−10617

$$NO_x + h^+(BSO) \rightarrow NO_3^- \quad (4)$$

In order to verify the quantitative transformation of NO in nitrite and or nitrate (NO_x^-), the nitrogen mass balance was calculated between the amount of produced final product NO_x^- and NO_2 intermediate and the amount of NO removed from air after 60 min of irradiation. As shown in Figure S8, the BSO-12 shows the maximum amount in NO conversion and accumulation of NO_x^- with lower NO_2 yield than BSO-24 and BSO-36. The results appearing may be due to the rapid charge separation and sufficient amount of strong oxidative species, while the BSO with smaller particle size could potentially reduce the chance of charge recombination and increase the surface area and amount of oxidative species leading to a more complete oxidation of NO. The inserted table showed the calculated and measured [NO_x^-] values. Compared with the calculated values, the measured values are lower, which could be attributed to the particle of NO_x^- on the surface of catalysts drawn airflow away. Moreover, there may be some new species undetectable by chemiluminescent NO_x analyzer and ion chromatography.[11]

6. CONCLUSION

In summary, nanocrystalline $Bi_2Sn_2O_7$ samples were successfully synthesized through a facile hydrothermal route, and the associated photocatalytic NO removal mechanism was investigated in detail. Synthesis time was a key factor influencing the microstructures of the resulting $Bi_2Sn_2O_7$ samples, which eventually affected their photocatalytic activities. The BSO-12 sample exhibited superior activity to those of BSO-24 and BSO-36 samples because of its smaller particle size, improved optical absorption capability, high specific surface area, and rapid separation/diffusion rates of the photogenerated charge carriers. Results of trapping experiments of active species and DMPO-ESR characterization demonstrated that the photogenerated holes and $\cdot O_2^-$ radicals were involved in photocatalytic NO degradation. This study showed that nanocrystalline $Bi_2Sn_2O_7$ is a promising photocatalyst for indoor air purification.

■ ASSOCIATED CONTENT

Supporting Information

The Supporting Information is available free of charge on the ACS Publications website at DOI: 10.1021/acs.iecr.6b02514.

Spectral composition of the light source; XRD patterns of the $Bi_2Sn_2O_7$ samples synthesized at 8 h; IR spectrum of the as-prepared BSO-12, BSO-24, and BSO-36 samples; comparison of the NO conversion rate and NO_2 yield; XRD patterns of $Bi_2Sn_2O_7$ before and after repeated irradiation and photoluminescence spectra of the as-prepared $Bi_2Sn_2O_7$ samples at room temperature; the conversion amount of NO, the produced amount of NO_2 and NO_x^-; the calculated and measured [NO_x^-] values; BET surface areas, pore volume, pore size, particle size, and optical band gap (PDF)

■ AUTHOR INFORMATION

Corresponding Authors

*Y.H.: e-mail, huangyu@ieecas.cn; tel, 86-29-6233 6261.
*J.-j.C.: e-mail, cao@loess.llqg.ac.cn; tel, 86-29-6233 6205.

Notes

The authors declare no competing financial interest.

■ ACKNOWLEDGMENTS

This research was financially supported by the National Science Foundation of China (Grants 41401567 and 41573138). It was also partially supported by the Research Grants Council of Hong Kong (Grant PolyU 152083/14E) and the research grant of Early Career Scheme (Grant ECS 809813) from the Research Grant Council, Hong Kong SAR Government. Y.H. is also supported by the "Hundred Talent Program" of the Chinese Academy of Sciences.

■ REFERENCES

(1) Gandolfo, A.; Bartolomei, V.; Alvarez, E. G.; Tlili, S.; Gligorovski, S.; Kleffmann, J.; Wortham, H. The effectiveness of indoor photocatalytic paints on NO*x* and HONO levels. *Appl. Catal., B* **2015**, *166*, 84−90.

(2) Ao, C.; Lee, S. C.; Yu, J. Z.; Xu, J. H. Photodegradation of formaldehyde by photocatalyst TiO_2: effects on the presences of NO, SO_2 and VOCs. *Appl. Catal., B* **2004**, *54* (1), 41−50.

(3) Lee, S. C.; Wang, B. Characteristics of emissions of air pollutants from burning of incense in a large environmental chamber. *Atmos. Environ.* **2004**, *38* (7), 941−951.

(4) Wang, B.; Lee, S. C.; Ho, K. F. Characteristics of carbonyls: Concentrations and source strengths for indoor and outdoor residential microenvironments in China. *Atmos. Environ.* **2007**, *41* (13), 2851−2861.

(5) Huang, Y.; Ho, S. S. H.; Ho, K. F.; Lee, S.; Yu, J. Z.; Louie, P. K. K. Characteristics and health impacts of VOCs and carbonyls associated with residential cooking activities in Hong Kong. *J. Hazard. Mater.* **2011**, *186* (1), 344−351.

(6) Chao, C. Y. H. Comparison between indoor and outdoor air contaminant levels in residential buildings from passive sampler study. *Environ. Build.* **2001**, *36* (9), 999−1007.

(7) Fischer, S. L.; Koshland, C. P. Daily and peak 1 h indoor air pollution and driving factors in a rural Chinese village. *Environ. Sci. Technol.* **2007**, *41* (9), 3121−3126.

(8) Lin, J. T.; McElroy, M. B.; Boersma, K. F. Constraint of anthropogenic NO*x* emissions in China from different sectors: a new methodology using multiple satellite retrievals. *Atmos. Chem. Phys.* **2010**, *10* (1), 63−78.

(9) Huang, Y.; Ho, W.; Lee, S.; Zhang, L.; Li, G.; Yu, J. C. Effect of carbon doping on the mesoporous structure of nanocrystalline titanium dioxide and its solar-light-driven photocatalytic degradation of NO*x*. *Langmuir* **2008**, *24* (7), 3510−3516.

(10) Huang, Y.; Ho, W.; Ai, Z.; Song, X.; Zhang, L.; Lee, S. Aerosol-assisted flow synthesis of B-doped, Ni-doped and B-Ni-codoped TiO_2 solid and hollow microspheres for photocatalytic removal of NO. *Appl. Catal., B* **2009**, *89* (3−4), 398−405.

(11) Ai, Z.; Ho, W.; Lee, S.; Zhang, L. Efficient Photocatalytic Removal of NO in Indoor Air with Hierarchical Bismuth Oxybromide Nanoplate Microspheres under Visible Light. *Environ. Sci. Technol.* **2009**, *43* (11), 4143−4150.

(12) Huang, Y.; Ai, Z.; Ho, W.; Chen, M.; Lee, S. Ultrasonic spray pyrolysis synthesis of porous Bi_2WO_6 microspheres and their visible-light-induced photocatalytic removal of NO. *J. Phys. Chem. C* **2010**, *114* (14), 6342−6349.

(13) Quan, X.; Yang, S. G.; Ruan, X. L.; Zhao, H. M. Preparation of titania nanotubes and their environmental applications as electrode. *Environ. Sci. Technol.* **2005**, *39* (10), 3770−3775.

(14) Dong, F.; Wang, H.; Wu, Z. One-step "green" synthetic approach for mesoporous C-doped titanium dioxide with efficient visible light photocatalytic activity. *J. Phys. Chem. C* **2009**, *113* (38), 16717−16723.

(15) Dong, F.; Guo, S.; Wang, H.; Li, X.; Wu, Z. Enhancement of the visible light photocatalytic activity of C-doped TiO_2 nanomaterials prepared by a green synthetic approach. *J. Phys. Chem. C* **2011**, *115* (27), 13285−13292.

DOI: 10.1021/acs.iecr.6b02514
Ind. Eng. Chem. Res. 2016, 55, 10609−10617

(16) Daghrir, R.; Drogui, P.; Robert, D. Modified TiO_2 for environmental photocatalytic applications: a review. *Ind. Eng. Chem. Res.* **2013**, *52* (10), 3581−3599.
(17) Zhang, L.; Xu, T.; Zhao, X.; Zhu, Y. Controllable synthesis of Bi_2MoO_6 and effect of morphology and variation in local structure on photocatalytic activities. *Appl. Catal., B* **2010**, *98* (3), 138−146.
(18) Kudo, A.; Omori, K.; Kato, H. A novel aqueous process for preparation of crystal form-controlled and highly crystalline $BiVO_4$ powder from layered vanadates at room temperature and its photocatalytic and photophysical properties. *J. Am. Chem. Soc.* **1999**, *121* (49), 11459−11467.
(19) Walsh, A.; Watson, G. W.; Payne, D. J.; Atkinson, G.; Egdell, R. G. A theoretical and experimental study of the distorted pyrochlore $Bi_2Sn_2O_7$. *J. Mater. Chem.* **2006**, *16* (34), 3452−3458.
(20) Wu, J.; Huang, F.; Lü, X.; Wan, D.; Xu, F. Improved visible-light photocatalysis of nano-$Bi_2Sn_2O_7$ with dispersed s-bands. *J. Mater. Chem.* **2011**, *21* (11), 3872−3876.
(21) Tian, Q. F.; Zhuang, J. D.; Wang, J. X.; Xie, L. Y.; Liu, P. Novel photocatalyst, $Bi_2Sn_2O_7$, for photooxidation of As(III) under visible-light irradiation. *Appl. Catal., A* **2012**, *425*, 74−78.
(22) Suzuki, M.; Noyori, R.; Långström, B.; Watanabe, Y. Molecular Design of Prostaglandin Probes in Brain Research: High, Specific Binding to a Novel Prostacyclin Receptor in the Central Nervous System. *Bull. Chem. Soc. Jpn.* **2000**, *73* (5), 1053−1070.
(23) Evans, I. R.; Howard, J. A. K.; Evans, J. S. O. Alpha-$Bi_2Sn_2O_7$-a 176 atom crystal structure from powder diffraction data. *J. Mater. Chem.* **2003**, *13* (5), 2098−2103.
(24) Gribb, A. A.; Banfield, J. F. Particle size effects on transformation kinetics and phase stability in nanocrystalline TiO_2. *Am. Mineral.* **1997**, *82* (7), 717−728.
(25) Pascuta, P.; Culea, E. FTIR spectroscopic study of some bismuth germanate glasses containing gadolinium ions. *Mater. Lett.* **2008**, *62* (25), 4127−4129.
(26) Li, G.; Zhang, D.; Yu, J. C. Ordered mesoporous $BiVO_4$ through nanocasting: A superior visible light-driven photocatalyst. *Chem. Mater.* **2008**, *20* (12), 3983−3992.
(27) Weller, H.; Schmidt, H.; Koch, U.; Fojtik, A.; Baral, S.; Henglein, A.; Kunath, W.; Weiss, K.; Dieman, E. Photochemistry of colloidal semiconductors. Onset of light absorption as a function of size of extremely small CdS particles. *Chem. Phys. Lett.* **1986**, *124* (6), 557−560.
(28) Almquist, C. B.; Biswas, P. Role of synthesis method and particle size of nanostructured TiO_2 on its photoactivity. *J. Catal.* **2002**, *212* (2), 145−156.
(29) Serpone, N.; Lawless, D.; Khairutdinov, R. Size effects on the photophysical properties of colloidal anatase TiO_2 particles: size quantization versus direct transitions in this indirect semiconductor. *J. Phys. Chem.* **1995**, *99* (45), 16646−16654.
(30) Henglein, A. Small-particle research: physicochemical properties of extremely small colloidal metal and semiconductor particles. *Chem. Rev.* **1989**, *89* (8), 1861−1873.
(31) Christensen, P. A.; Curtis, T. P.; Egerton, T. A.; Kosa, S. A. M.; Tinlin, J. R. Photoelectrocatalytic and photocatalytic disinfection of E-coli suspensions by titanium dioxide. *Appl. Catal., B* **2003**, *41* (4), 371−386.
(32) Liao, G.; Chen, S.; Quan, X.; Chen, H.; Zhang, Y. Photonic crystal coupled TiO_2/polymer hybrid for efficient photocatalysis under visible light irradiation. *Environ. Sci. Technol.* **2010**, *44* (9), 3481−3485.
(33) Hu, R.; Xiao, X.; Tu, S.; Zuo, X.; Nan, J. Synthesis of flower-like heterostructured β-Bi_2O_3/$Bi_2O_2CO_3$ microspheres using $Bi_2O_2CO_3$ self-sacrifice precursor and its visible-light-induced photocatalytic degradation of o-phenylphenol. *Appl. Catal., B* **2015**, *163*, 510−519.
(34) Cardona, M. Optical Properties and Band Structure of $SrTiO_3$ and $BaTiO_3$. *Phys. Rev.* **1965**, *140* (2A), A651.
(35) Spagnol, V.; Sutter, E.; Debiemme-Chouvy, C.; Cachet, H.; Baroux, B. EIS study of photo-induced modifications of nano-columnar TiO_2 films. *Electrochim. Acta* **2009**, *54* (4), 1228−1232.
(36) Dong, F.; Li, Q.; Sun, Y.; Ho, W. K. Noble Metal-Like Behavior of Plasmonic Bi Particles as a Cocatalyst Deposited on $(BiO)_2CO_3$ Microspheres for Efficient Visible Light Photocatalysis. *ACS Catal.* **2014**, *4* (12), 4341−4350.
(37) Li, Z.; Dong, T.; Zhang, Y.; Wu, L.; Li, J.; Wang, X.; Fu, X. Studies on $In(OH)_yS_z$ solid solutions: syntheses, characterizations, electronic structure, and visible-light-driven photocatalytic activities. *J. Phys. Chem. C* **2007**, *111* (12), 4727−4733.
(38) Yin, S.; Liu, B.; Zhang, P.; Morikawa, T.; Yamanaka, K.; Sato, T. Photocatalytic oxidation of NO*x* under visible LED light irradiation over nitrogen-doped titania particles with iron or platinum loading. *J. Phys. Chem. C* **2008**, *112* (32), 12425−12431.
(39) Ohko, Y.; Nakamura, Y.; Fukuda, A.; Matsuzawa, S.; Takeuchi, K. Photocatalytic oxidation of nitrogen dioxide with TiO_2 thin films under continuous UV-light illumination. *J. Phys. Chem. C* **2008**, *112* (28), 10502−10508.

DOI: 10.1021/acs.iecr.6b02514
Ind. Eng. Chem. Res. 2016, 55, 10609−10617